# Analysis of RC Slab-beam-column Sub-assemblages Subjected to Bi-directional Lateral Cyclic Loading Using a New 3D Macro Element

Suhee Kim[a], Fumio Kusuhara[b] and Hitoshi Shiohara[c]

## SUMMARY

An existing two-dimensional macro-element for reinforced concrete beam-column joints is extended to a three-dimensional macro-element. The three-dimensional macro-element for beam-column joints consists of six rigid interface plates and uniaxial springs for concrete, steel and bond-slip, which model the inside of a beam-column joint. The mechanical models for the materials and the stiffness equation for the springs are also presented. To validate the model, test results from three slab-beam-column subassemblies subjected to bi-lateral cyclic load are used. It is revealed that the new joint model is capable to capture the strength of beam-column joints and the bi-directional interaction in joint shear response, including the concentration of damage in the beam-column joint, the pinching nature in hysteretic behavior, the stiffness degradation and strength deterioration resulting from cyclic and bi-directional loading.

Key Words: reinforced concrete; slab-beam-column sub-assemblage; beam-column joint; bidirectional lateral load; macro element

## 1. INTRODUCTION

Under earthquake loading, beam-column joints in two-way ductile-moment space frames are subjected to bi-directional lateral cyclic loading. To assess a structural system using nonlinear response history analysis, a mathematical model is required that is capable of accurately simulating the nonlinear cyclic response of beam-column joints subject to bi-directional lateral loading interaction. However, no three-dimensional (3D) model of practical nonlinear response simulation considering bi-directional interaction has been available for reinforced concrete (RC) beam-column joints. As a result, to the best of our knowledge, the impact on beam-column joints response when subjected to bidirectional lateral loading has not been reported.

Since the late 1990s, two-dimensional (2D) models for RC beam-column joints have been developed. These models were due to the necessity of assessing the seismic performance of old and existing RC buildings. They usually consist of rigid elements and rotational springs; e.g., [1, 2, 3, 4 and 5]. However, there is no direct path to extend these 2D models to simulate the bi-directional response of beam-column joints because of the complexity of such a 3D model and

---

[a] Mitsubishi Chemical Engineering Corporation, Engineering Division, Tokyo, Japan
[b] Department of Architecture and Design, Nagoya Institute of Technology, Nagoya, Japan
[c] Department of Architecture, School of Engineering, the University of Tokyo, Tokyo, Japan

the difficulty of capturing the two-way interaction of stiffness and strength deterioration in a beam-column joint. Such models also need the calibration of the backbone curve of a shear stress-strain relationship under bidirectional loading by 3D tests. The 3D nonlinear finite element analysis of a full structure is not practical because the dynamic non-linear analyses of structural systems are computationally extremely demanding, in particular for cyclic bi-directional loading.

The authors have been developing a mechanical model that captures the nonlinear behavior of RC beam-column joints [6]. Based on the results of the study, the first macro-element for beam-column joints was proposed for 2D beam-column joints by Tajiri and Shiohara [7]. Kusuhara simplified the model to simulate 2D beam-column joint tests including four interior and four exterior joints [8] that exhibited joint hinging behavior. The joint hinging is a type of joint failure mechanism recognized recently, theoretically predicted [9], and experimentally verified [10] by the authors, in which the beam-column joint reaches maximum strength by the tensile yielding of longitudinal bars in both the horizontal and vertical directions within the joint shear panel. The joint hinging mechanism is known to exhibit lower strength than predicted by the flexural theory of the section and severely pinched hysteretic characteristics. They compared the simulation and measured response and obtained a result where the model satisfactorily captures the strength and hysteretic behavior of beam-column joints showing the joint hinging mechanism as well as beam hinging failure and joint shear failure. Hence, the macro-element presented here has an advantage, in that it can simulate the joint hinging mechanism, which is neglected by all existing 2D joint models along with the beam hinging and joint shear failure. Although the macro-element model requires a moderate amount of computational effort, it has a great advantage over existing joint models in that it can simulate the extremely realistic behavior of a beam-column joint.

To date, few experimental data are reported for RC 3D slab-beam-column sub-assemblages, including [11, 12, 13 and 14]. One of the test series, which seems to have exhibited a joint hinging mechanism, was subjected to an intensive bi-directional lateral loading path, performed by Kurose et al. at the University of Texas. They tested three slab-beam-column sub-assemblages statically loaded under uniaxial or bidirectional lateral loading to failure [12]. They reported that the longitudinal bars in the beams and the joint hoops yielded during the early load cycles and that the longitudinal bars in the column also yielded in later load cycles. Large deformation was measured in the beam-column joints. It is also reported that specimens under bidirectional lateral loading exhibited strength loss more rapidly than specimens subjected to unidirectional loading. Considering bi-directional interaction in a beam-column joint is necessary to simulate such behavior.

In this paper, first, the 2D macro-element for beam-column joints is extended to 3D macro-elements. Then, the tests by Kurose et al. are used to validate the 3D macro-element proposed here. The beam-column joints of the slab-beam-column sub-assemblages are modeled with the 3D macro-element, and the correlation of simulation and test results are examined.


## 2. MATHEMATICAL FORMULATION OF A 3D BEAM-COLUMN JOINT

### 2.1 Overview
The macro-element presented herein was developed for RC beam-column joints in a space frame that joins horizontal beams in two orthogonal directions with vertical columns. The term of macro-element is used here to refer to structural elements consisting of assemblage of 1D decoupled springs with force-displacement relationships rather than stress-strain relationships.

The boundary of the beam-column joint is modeled as six separate rigid plates at the center of which are given nodal degrees of freedom (DOFs) for three translational and three rotational DOFs. As a result, the macro-element has 36 external DOFs in total. The six nodes are shared with adjacent beams and columns constituting a beam-column joint sub-assemblage. The concrete uniaxial springs in the beam-column joint are placed uniformly in 9 directions in 3D space, the cross-sectional area for which was chosen to be the same as the tributary area perpendicular to each direction. The steel uniaxial springs are placed in the horizontal or vertical direction at the same location of the actual reinforcing bars including transverse reinforcement in the joint. The properties of the concrete and steel springs are determined based on the uniaxial non-linear mechanical properties of the materials. The bond slip springs consider the interaction of longitudinal reinforcement and the surrounding concrete.

In the 3D joint macro-element, joint shear is resisted by the truss action of inclined concrete springs in compression and the reinforcing steel springs in tension, whereas the moments from adjacent beams and columns also need to be transferred by the diagonal compression in the springs and steel springs in tension. The axial load in the upper and the lower column was mainly transferred by the vertical concrete and steel springs. Moments under gravity load on the opposite beam ends are balanced at the joint by compression in the horizontal concrete springs and tension in the horizontal steel springs. Consequently, the macro-element reflects the general interaction of axial force, joint shear and moment transfer in the beam-column joints subjected to lateral force, as well as the gravity load transferred from the beams to the column.
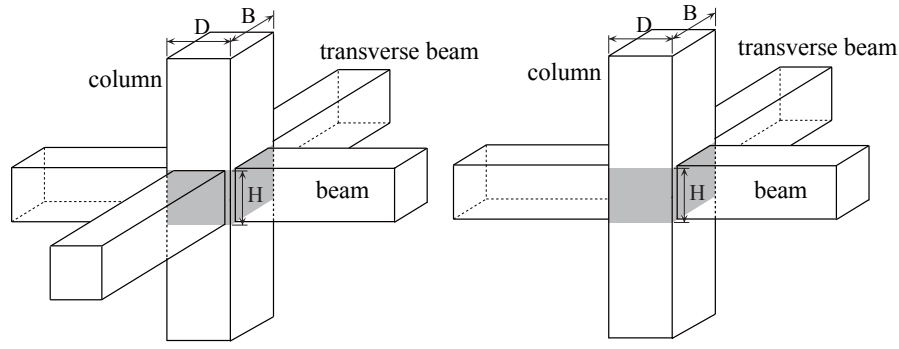


(a) 3-D beam-column joints
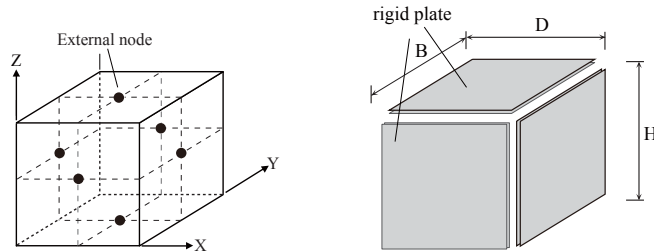


(b) DOF-representing node of 3D joint element and global coordinate system

**Fig. 1 –** Macro-element of a 3D beam-column joint

## 2.2 Location and connectivity of the elements

The geometry of a macro-element is defined by the following dimensions: depth of the column, $D$; width of the column, $B$; and height of the beam, $H$; as depicted in **Fig. 1 (a)**. It is not necessary for all six rigid plates to be connected to adjacent members as shown in **Fig. 1 (a)**. **Fig. 1(b)** shows the location of the external DOFs. The deformation in space is defined by the displacement of six rigid plates. In a frame analysis, the end of a line member and a beam-column joint plate share a single 6 DOF node.

The concrete springs are placed along the six diagonal directions and in three orthogonal directions, connecting the rigid boundary plates at both ends as shown in **Fig. 2**. In the linearly elastic range of concrete, this multi-directional concrete spring causes an overestimation of the stiffness of concrete. However, considering the nonlinear property of concrete subject to tensile-compression strain fields after cracking, only the selective springs in the direction of principal axial strain can resist the compression. Therefore, it is not necessarily overestimating the stiffness of cracked concrete. The steel springs are placed in three directions, connecting a rigid plate and an internal node with one DOF in the spring direction, which is connected to the rigid plates in its vicinity with dimensionless bond-slip springs.
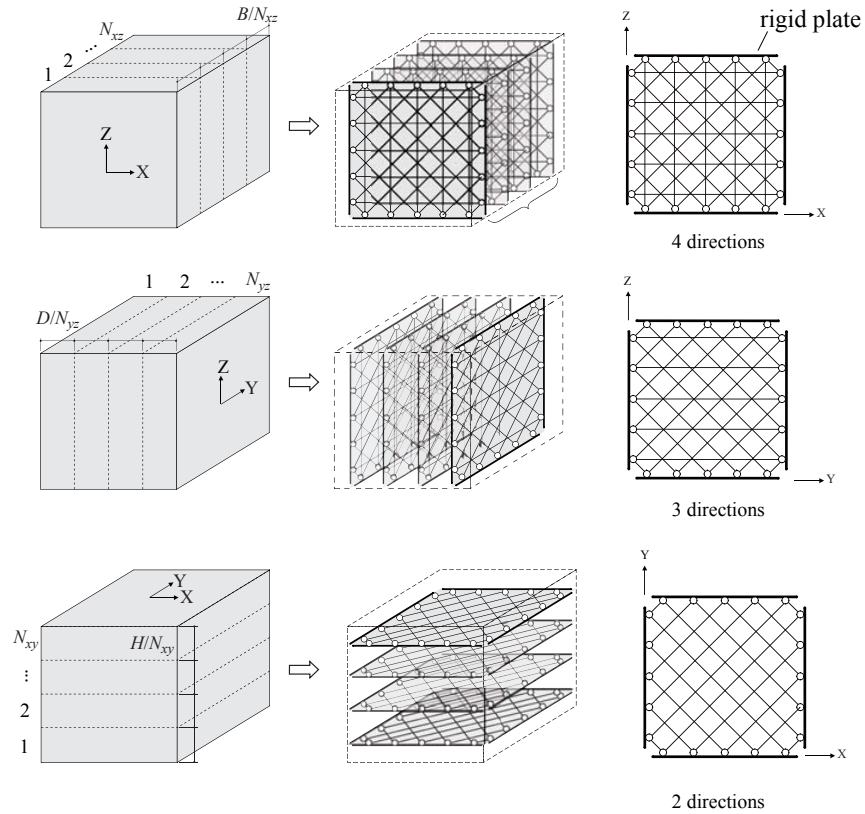


Fig. 2 – Nine directions of concrete springs and their tributary areas

## 2.3 Concrete springs

Concrete in a beam-column joint is sliced like a fiber model. A single layer of the concrete consists of two diagonals and the orthogonal springs shown in **Fig. 3**. Each of the concrete springs is modeled as uniaxial concrete bars. The length, $L_n$, is the distance between the two ends,

and the cross sectional area $A_n$ is $A_n = d_n w$, where $d_n$ is the tributary width of the concrete spring, and $w$ is the thickness of a single concrete layer. The section area $A_n$ of the orthogonal concrete springs are $Hw/N$ and $Dw/N$, where $N$ is the number of the division, as shown in **Fig. 3 (b)**, and **Fig. 3 (c)**.



$$A_n = d_n \times w = \frac{DH}{N\sqrt{D^2 + H^2}} \times \frac{B}{N_c} \qquad A_n = d_n \times w = \frac{H}{N} \times \frac{B}{N_c} \qquad A_n = d_n \times w = \frac{D}{N} \times \frac{B}{N_c}$$

$$L_n = \frac{2(N-m)+1}{2N}\sqrt{D^2 + H^2} \qquad L_n = D \qquad L_n = H$$

( $N_c$ : number of parallel concrete layers, $m$ (=1, 2…N) : uniaxial spring number)

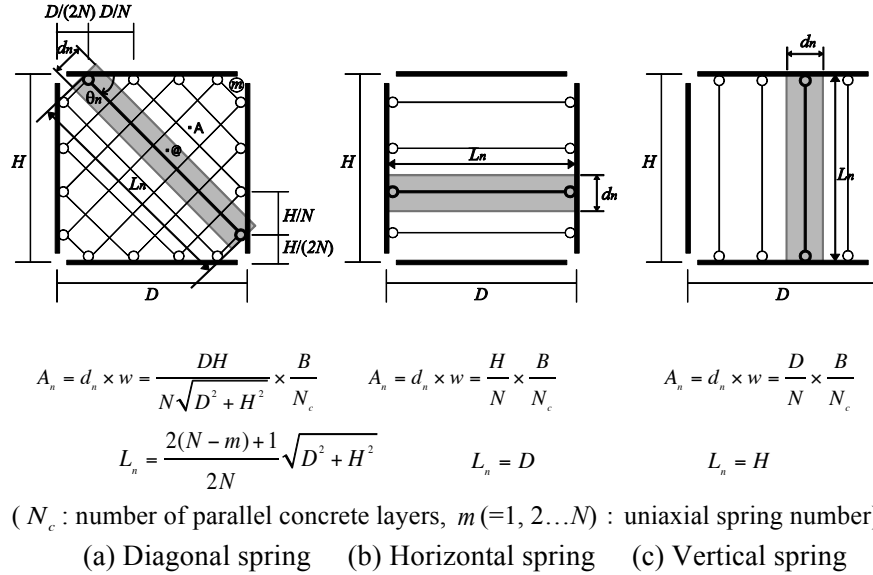(a) Diagonal spring    (b) Horizontal spring    (c) Vertical spring

**Fig. 3** – Properties of concrete springs

## 2.4 Reinforcing steel springs

The steel springs consider the sectional area of the reinforcing bars. The steel spring length is modified to consider the effect of the slip out of longitudinal bars from beams or columns. The pull-out of reinforcing bars from beams or columns into the beam-column joint interface causes under estimation of the chord rotation compared to that estimated by the integration of the theoretical moment-curvature relation of the section. To adjust this effect, the length of a reinforcement spring $L_n$ in the joint macro-element is modified as $L_n = L_e + l_s$, where $L_e$ is the actual distance between the two ends of the steel spring, and $l_s$ is the additional length contributing to the counting for pull-out deformation, taken as half of the maximum distance between the top and bottom rebar of the beam or column. The effective pull-out length $l_s$ is added to consider the difference of the total tensile elongation of the tensile steel calculated from flexural theory and the assumed distribution considering the tension shift of tensile steel strain due to the shear resisting mechanism as shown in **Fig. 4(a)**.

## 2.5 Bond-slip springs

Bond-slip along beam and column longitudinal reinforcing bars is explicitly modeled by bond springs that connect the inner node at the midpoint of the reinforcing bar to an adjacent rigid plate as shown in **Fig. 4(b)**. For the corner column, longitudinal bars, two bond springs are placed onto two neighboring orthogonal rigid plates because the force is transferred via bond from those bars. Bond force is defined as $\tau A_s$, where $\tau$ is the bond stress, and $A_s$ is the surface area of the longitudinal reinforcement, which does not include the contribution of $l_s$, the

effective length for longitudinal bars. Uniaxial springs representing slab bars within effective slab width and transverse reinforcements in a beam-column joint are simplified as one steel spring placed at the mid-height of the macro-element with no bond spring placed between the transverse reinforcements and concrete as shown in **Fig. 4(c)**.
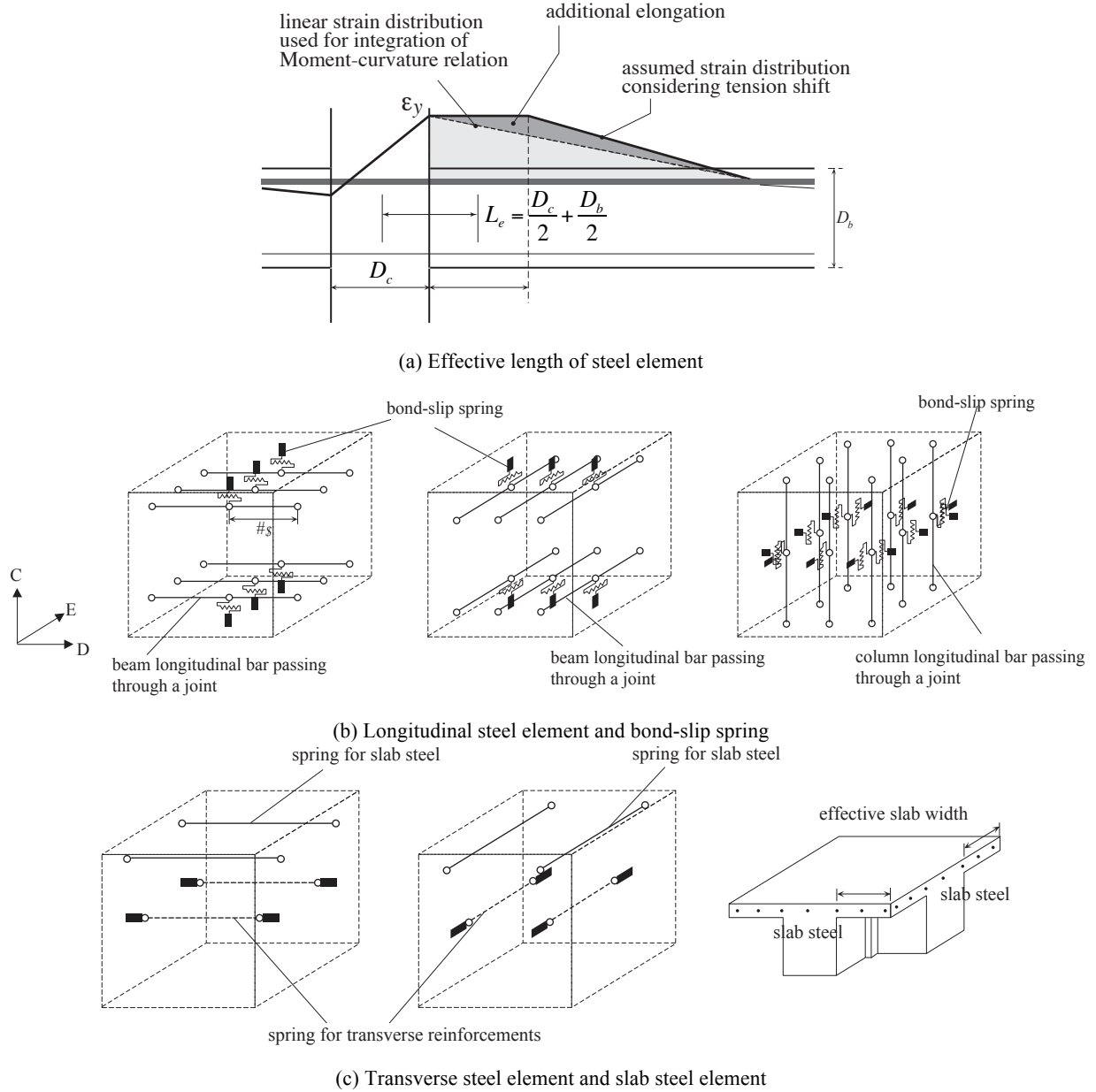


(a) Effective length of steel element



(b) Longitudinal steel element and bond-slip spring



(c) Transverse steel element and slab steel element

**Fig. 4** – Steel and bond-slip springs

## 2.6 Compatibility equations

Compatibility equations define the generalized displacements (displacements and rotations) at uniaxial spring ends for given generalized displacements at external DOFs.

When one end (1st-end) of a spring is connected to the $i$-th rigid plate and the other end (2nd-end) is connected to the $j$-th rigid plate, the displacements at the two ends of the spring are explicitly defined by the rigid plate constraint imposed at the joint boundaries and the general displacements (i.e., displacements and rotations) of nodes $i$ and $j$. The relationship between the nodal displacements of a spring $\mathbf{d}_{12}$ [6x1] and the displacements of DOF-representing nodes $\mathbf{d}_{ij}$ [12x1] is generally expressed in the global coordinate system as:

$$\begin{Bmatrix} \mathbf{d}_1 \\ \mathbf{d}_2 \end{Bmatrix} = \begin{bmatrix} \mathbf{R}_{1i}{}^t & \mathbf{0} \\ \mathbf{0} & \mathbf{R}_{2j}{}^t \end{bmatrix} \begin{Bmatrix} \mathbf{d}_i \\ \mathbf{d}_j \end{Bmatrix} \quad \text{or:} \quad \left( \mathbf{d}_{12} = \mathbf{R}_{12ij}^t \mathbf{d}_{ij} \right) \tag{1}$$

where, $\mathbf{d}_1$ and $\mathbf{d}_2$ are the three displacements, at constrained nodes 1 and 2 of the spring in the global coordinate system; $\mathbf{d}_i$ and $\mathbf{d}_j$ are the six generalized displacements (like $\mathbf{d}_1$ and $\mathbf{d}_2$) at the retained nodes $i$ and $j$ in the global coordinate system; $\mathbf{R}_{1i}$ and $\mathbf{R}_{2j}$ are the constraint matrices defined by their relative position between constrained nodes 1 and 2 and retained nodes $i$ and $j$ as:

$$\mathbf{R}_{1i} = \begin{bmatrix} 1 & 0 & 0 \\ 0 & 1 & 0 \\ 0 & 0 & 1 \\ 0 & -ez_{1i} & ey_{1i} \\ ez_{1i} & 0 & -ex_{1i} \\ -ey_{1i} & ex_{1i} & 0 \end{bmatrix} \quad \mathbf{R}_{2j} = \begin{bmatrix} 1 & 0 & 0 \\ 0 & 1 & 0 \\ 0 & 0 & 1 \\ 0 & -ez_{2j} & ey_{2j} \\ ez_{2j} & 0 & -ex_{2j} \\ -ey_{2j} & ex_{2j} & 0 \end{bmatrix} \tag{2}$$

where $ex_{1i}$, $ey_{1i}$ and $ez_{1i}$ are the distance from node $i$ to node 1 in the $X$, $Y$, and $Z$-axis directions, respectively; and similarly $ex_{2i}$, $ey_{2i}$ and $ez_{3i}$ are the distance from node $j$ to node 2 in the $X$, $Y$, and $Z$-axis directions, respectively, as illustrated in **Fig. 5**.
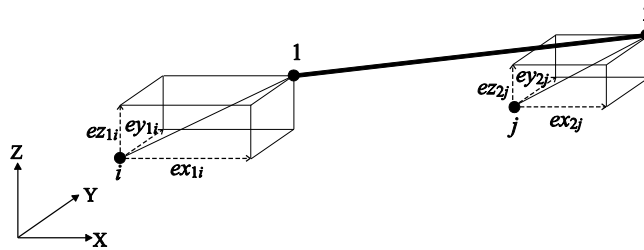


**Fig. 5** – Compatibility

With the coordinate transformation matrix $\mathbf{\Gamma}_{12}$ [3x3], $\mathbf{d}_{12}$, the nodal displacements at the end of the spring in the global coordinate system [6x1] are transformed to $\mathbf{d}'_{12}$ in the local coordinate system [6x1], the relationship of which is described as follows:

$$\left\{ \begin{array}{c} \mathbf{d}_1' \\ \mathbf{d}_2' \end{array} \right\} = \left[ \begin{array}{cc} \boldsymbol{\Gamma}_{12}{}^t & 0 \\ 0 & \boldsymbol{\Gamma}_{12}{}^t \end{array} \right] \left\{ \begin{array}{c} \mathbf{d}_1 \\ \mathbf{d}_2 \end{array} \right\} \quad \text{or:} \quad \left( \mathbf{d}_{12}' = \boldsymbol{\Gamma}_{12}{}^t \mathbf{d}_{12} \right) \tag{3}$$

where $\mathbf{d}_1'$ and $\mathbf{d}_2'$ are the three displacements at the constrained nodes 1 and 2 at the ends of a spring in the local coordinate system. Axial deformation of a uniaxial spring element $\mathbf{e}_{12}$ can be expressed as:

$$\mathbf{e}_{12} = \left[ \begin{array}{cccccc} -1 & 0 & 0 & 1 & 0 & 0 \end{array} \right] \left\{ \begin{array}{c} \mathbf{d}_1' \\ \mathbf{d}_2' \end{array} \right\} \quad \text{or:} \quad \left( \mathbf{e}_{12} = \mathbf{H}^t \mathbf{d}_{12}' \right) \tag{4}$$

Combining the above relationships, the relation of $\mathbf{e}_{12}$, the axial deformation of a spring, and $\mathbf{d}_{ij}$, the generalized displacements of external joint nodes $i$ and $j$, is given as follows:

$$\mathbf{e}_{12} = \mathbf{H}^t \boldsymbol{\Gamma}^t \mathbf{R}_{12ij}{}^t \left\{ \begin{array}{c} \mathbf{d}_i \\ \mathbf{d}_j \end{array} \right\} \quad \text{or:} \quad \left( \mathbf{e}_{12} = \mathbf{C}_{12ij}{}^t \mathbf{d}_{ij} \right) \tag{5}$$

The compatibility matrix, $\mathbf{C}_{12ij} \left( = \mathbf{R}_{12ij} \boldsymbol{\Gamma}_{12} \mathbf{H} \right)$ [12x1], is used to formulate the stiffness equations for the macro-element in the global coordinate system.

When one end (1st-end) of a spring is connected to a rigid plate and the other end (2nd-end) is connected to an internal node, such as the case of steel springs for longitudinal bars or the bond slip springs, the displacement at the one end of the spring is the defined displacement of an external node, and the displacement at the other end is of an internal node. Moreover, the axial deformation $\mathbf{e}$ of the springs is derived similarly, using a compatibility matrix $\mathbf{C}$, constraint matrix $\mathbf{R}$, coordinate transformation matrix $\boldsymbol{\Gamma}$, and an equilibrium matrix $\mathbf{H}$, which are not shown here.

## 2.7 The stiffness equation

The relationship between the axial deformation of uniaxial springs and the nodal DOF of a 3D joint macro-element including the external and internal nodes can be written as follows:

$$\mathbf{e} = \mathbf{C}^t \mathbf{d} \tag{6}$$

where $\mathbf{e}$ is a vector of axial deformation of the uniaxial springs with a matrix size of $[N_m \times 1]$ ($N_m$ is the total number of uniaxial springs); $\mathbf{C}$ is a full compatibility matrix with the size of $[36 \times N_m]$; and $\mathbf{d}$ is a vector of the generalized nodal displacement of the six rigid plates with a matrix size of $[36 \times 1]$. From the principle of virtual work, the contra-gradient transformation for force is:

$$\mathbf{F} = \mathbf{C} \mathbf{p} \tag{7}$$

where $\mathbf{F}$ is a vector of the generalized nodal forces (three forces and three moments) for the six rigid plates with a matrix size of $[36 \times 1]$; and $\mathbf{p}$ is a vector of the axial force of the uniaxial

springs with a matrix size of $[N_m{\times}1]$. The axial force-deformation relationships for all uniaxial springs are expressed as:

$$\mathbf{p} = \mathbf{K_m e} \tag{8}$$

where $\mathbf{K_m}$ is a diagonal stiffness matrix with the matrix size of $[N_m{\times}N_m]$, and the $n$-th diagonal element of $\mathbf{K_m}$ is the axial stiffness of the $n$-th uniaxial spring, which is defined as:

$$k_n = E_n A_n / L_n \text{ (for concrete and steel springs)} \tag{9.1}$$

$$k_n = k_{\text{bond-slip}} \text{ (for bond slip springs)} \tag{9.2}$$

where $k_n$ is the tangential stiffness of the $n$-th uniaxial spring; and $E_n$, $A_n$, $L_n$ and $k_{\text{bond-slip}}$ are the tangential modulus of the material, the sectional area, the length of the spring, and the stiffness of bond-slip relation, respectively. Using the equations (6), (7), and (8) above, a stiffness equation for the 3D joint macro-element considering all the DOFs for external nodes and internal nodes can be obtained from:

$$\mathbf{F} = \mathbf{C K_m C^t d} \text{ or } \left( \mathbf{F} = \mathbf{Kd} \right) \tag{10}$$

A stiffness equation for the 3D joint macro-element for the DOFs of the external nodes can be obtained by a condensation of the stiffness matrix $\mathbf{K}$ to eliminate the DOFs of the internal nodes with an assumption that no external load is acting on the internal nodes within the 3D joint macro-element.


## 3. CONSTITUTIVE MODELS FOR MATERIAL

The constitutive models for the uniaxial stress-deformation relationships of concrete, steel and bond-slip are presented here.

### 3.1 Concrete in compression

**Figure 6 (a)** depicts the stress-strain relationship for concrete. The Kent and Park model [15] is adopted for the envelope curve in compression. The descending branch, after the compressive strength, is determined considering the length of the concrete spring. The post peak concrete crushing is localized to a finite region, and the dissipated work per unit area is a unique material parameter called the concrete compressive fracture energy. Therefore, the concrete post-peak of the concrete stress-strain response needs to be dependent on the length of the concrete spring. Hence, each post-peak slope parameter $Z_m$ of the concrete stress-strain relation is determined by considering the constant compressive fracture energy criterion. By considering the definition of the compressive fracture energy shown in **Fig. 6(b)**, the relation of the length and the concrete compressive fracture energy of a concrete spring is given as:

$$\frac{G_{fc}}{L_m} = \frac{1}{2}\left\{\varepsilon_0 - \left(\varepsilon_c - \frac{f_c}{E_c}\right)\right\}f_c \qquad (11)$$

where $G_{fc}$ is the concrete compressive fracture energy, the hatched area shown in **Fig. 6 (b)**; $L_m$ is the length of a concrete spring; $f_c$ is the compressive strength of concrete in MPa; $\varepsilon_c$ is the strain at compressive strength of concrete; and $\varepsilon_0$ is the strain of concrete at zero compressive strength. The concrete compressive fracture energy is assumed as $8.8\sqrt{f_c}$ in MPa, as was proposed by Nakamura et al. [16]. As the strain at compressive strength of concrete $\varepsilon_0$ is obtained by solving Eq. (11), the normalized post-peak slope $Z_m$ is calculated by Eq. (12):

$$Z_m = \frac{1}{\varepsilon_0 - \varepsilon_c} \qquad (12)$$

## 3.2 Concrete in tension

The ascending branch of the concrete stress-strain response is assumed to be linearly elastic in tension from zero to the tensile strength, and the softening slope is defined by the tensile fracture energy. An idealized tension-softening curve is shown in **Fig. 6 (c)**, and the fracture energy $G_{ft}$ is calculated by Eq. (13) [17]:

$$G_{ft} = 10\left(d_{max}\right)^{1/3} f_c^{1/3} \qquad (13)$$

where $d_{max}$ is the maximum size of aggregate in mm, and $f_c$ is the compressive strength of concrete in MPa.
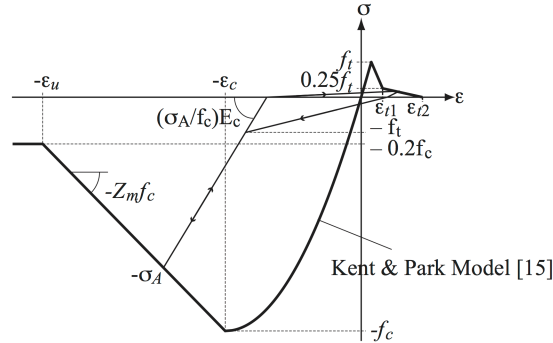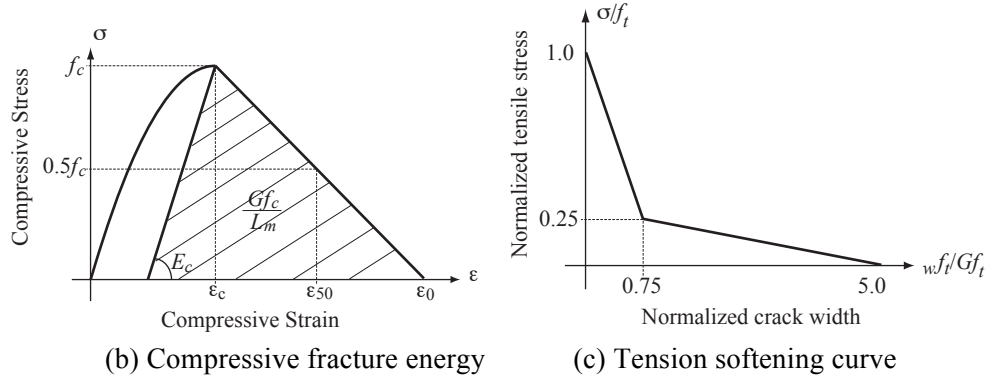


(a) Stress-strain relationship of concrete

(b) Compressive fracture energy      (c) Tension softening curve

**Fig. 6** – Constitutive model for concrete

### 3.3 Steel

The envelope curve of the stress-strain relation for reinforcing steel is assumed to be bilinear. The slope of the strain hardening branch is assumed to be equal to $0.001 E_s$, where $E_s$ is the elastic steel modulus. The hysteretic curves are masing-type with an unloading stiffness of $E_s$, where the Bauschinger effect is considered as simplified bilinear lines [7] as depicted in **Fig. 7**.
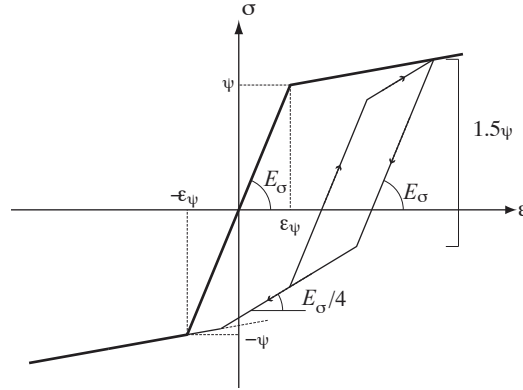


**Fig. 7** – Constitutive model for steel

### 3.4 Bond-slip

The envelope curve for the bond stress versus the slip response relation is a multi-linear simplification of the model by Eligehausen et al. [18] (**Fig. 8**). The hysteresis rules by Morita [19] are incorporated. The model parameters for the envelope curve are determined as those of the Good Bond Conditions of Confined Concrete in CEB-FIP Model Code [20].
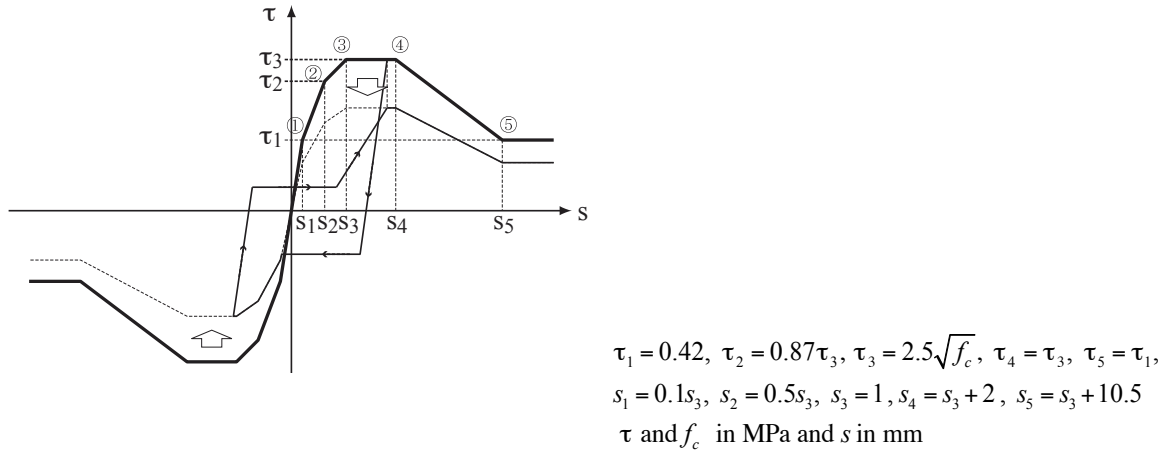
$$\tau_1 = 0.42, \ \tau_2 = 0.87\tau_3, \ \tau_3 = 2.5\sqrt{f_c}, \ \tau_4 = \tau_3, \ \tau_5 = \tau_1,$$

$$s_1 = 0.1s_3, \ s_2 = 0.5s_3, \ s_3 = 1, \ s_4 = s_3 + 2, \ s_5 = s_3 + 10.5$$

$$\tau \text{ and } f_c \text{ in MPa and } s \text{ in mm}$$

**Fig. 8 –** Bond stress versus slip relationship

## 4 MODELING OF LABORATORY SPECIMENS

### 4.1 Laboratory specimens

A test program of three full scale 3D slab-beam-column sub-assemblages was selected to validate the proposed 3D joint macro-element [12]. The geometry and the reinforcing details of the specimens are shown in **Fig. 9**. Specimen J1 is a one-way frame with a slab and without transverse beams. The column-to-beam strength ratio is approximately 1.2. Specimen J2 is a two-way moment frame sub-assemblage with two transverse beams framing into the continuous column. The column-to-beam strength ratios are approximately 1.4 in both directions. Specimen J3 is also a two-way moment resisting frame sub-assemblage with one continuous beam and one discontinuous beam framing into a continuous column. The column-to-beam strength ratio is approximately 2.0 for the normal direction where one discontinuous beam frames into the joint and approximately 1.2 for the transverse direction in which a continuous beam frames into the joint. (Note that 600 mm by 130 mm on each side of the beam was considered as the effective slab section that contributes to the beam strength to calculate the above ratios.)

The story height and the beam span are 165 in. (4,200 mm) and 192 in. (4,880 mm), respectively. It is reported [12] that the specimens were designed in accordance with the ACI318-83 [21] and the recommendation of ACI-ASCE 352 [22]. For all of the specimens, the nominal joint shear capacity to demand ratio is approximately 1.0; specifically, it is 0.9, 0.9 and 1.1 for the Specimens J1, J2 and J3, respectively. The lateral displacement trajectories for the tests are shown in **Fig. 10**. Specimen J1 was subjected to a unidirectional cyclic lateral displacement history, while Specimens J2 and J3 were subjected to bidirectional cyclic displacement histories. For all of the test specimens, no axial force was applied to the column. Normal strength concrete and normal strength reinforcing steel were used. The mechanical properties of the materials are listed in **Table 1**.

**Table 1**. Mechanical properties of materials by Kurose et al 1988 [12]

(a) Compressive strength of concrete in psi (MPa)

| Position | Specimen J1 | Specimen J2 | Specimen J3 |
|---|---|---|---|
| Slab, beam joint and lower column | 3500 (24) | 3700 (26) | 4700 (33) |
| Upper column | 3520 (24) | 3780 (26.5) | 3250 (22.5) |

(b) Rebar Strength in ksi (MPa)

| Bar | Yield point | Tensile strength |
|---|---|---|
| #3 | 80.8 (557) | 118.2 (814) |
| #4 | 79.7 (549) | 111.9 (771) |
| #6 | 74.2 (511) | 108.9 (750) |
| #7 | 65.6 (452) | 101.4 (698) |
| #8 | 67.2 (462) | 106.0 (730) |
| #9 | 66.6 (458) | 106.1 (731) |
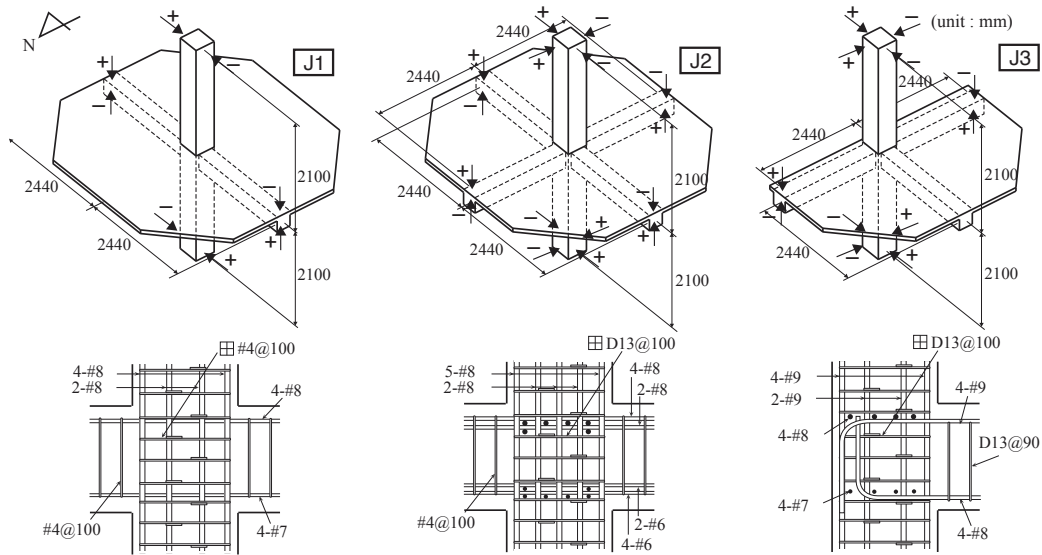


**Fig. 9 –** Geometry and joint reinforcing detail of reference specimens

13

(a) Specimen J1

(b) Specimen J2
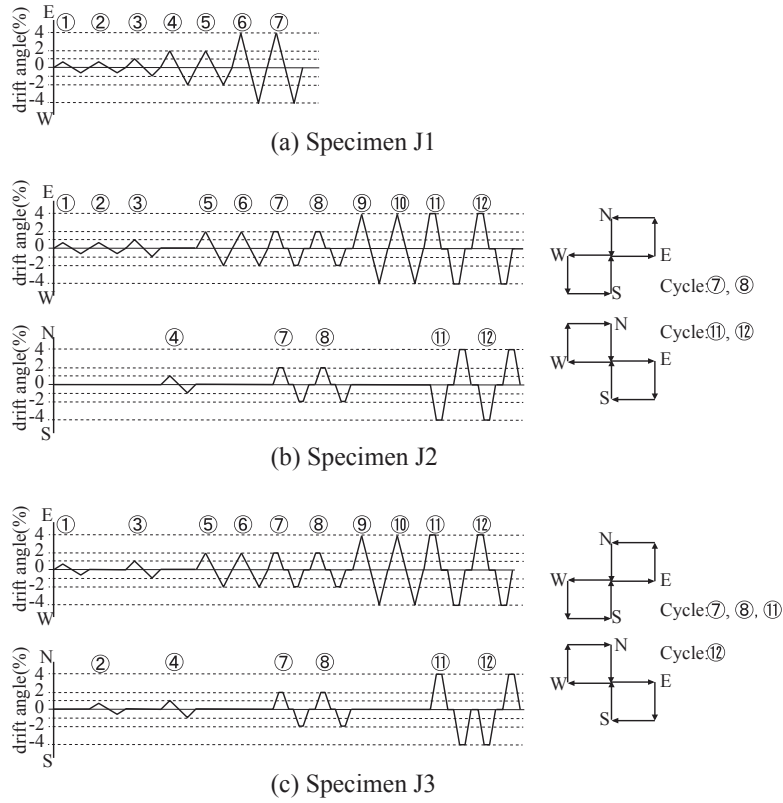
(c) Specimen J3

**Fig. 10 –** Loading histories



dimension in mm

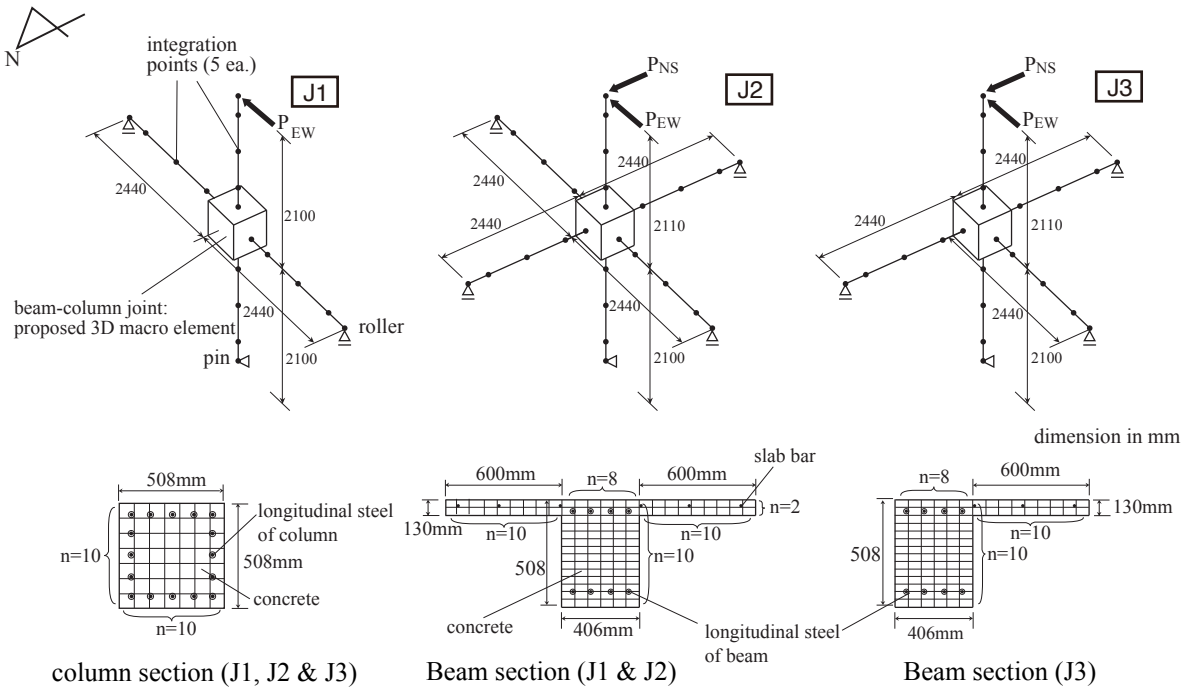column section (J1, J2 & J3)    Beam section (J1 & J2)    Beam section (J3)

**Fig. 11 –** Analytical model of reference specimens

**4.2 Model parameters**

The model parameters used for the concrete, steel and bond-slip constitutive models were determined from the material and geometry listed in **Table 1**. To determine the tensile fracture energy of concrete in Eq. 13, the maximum diameter of coarse aggregate is assumed to be 25 mm. **Figure 11** shows analytical representations of those specimens. The 3D joint macro-element described in the previous sections was used, and five divisions (i.e., $N = 5$) were used to define the layout of the concrete springs. As the differences in calculated results using five divisions or seven divisions were so little, results are shown for the case of five divisions.

Columns and beams were modeled using force-based elements with fiber-type cross-section models. The element resultant forces were computed using five fiber sections distributed along the length of the element, and the Gauss-Lobatto quadrature rule was used for the numerical integration [23] of the curvature along the element. The fiber sections were defined by uniaxial stress-strain relationships representing concrete and steel. The concrete and steel constitutive models for the fiber section are the same as in the joint. Thus, no explicit model is included for confinement of the concrete model. Additionally, using this formulation, plane sections are assumed to remain plane and perpendicular to the centroid axis. Thus, bond-slip behavior and shear deformation within the beams and columns are neglected. Finally, an elastic torsional response model is assumed for the beams and columns.

For all the specimens, the slab is modeled by a simple approach of the T-shape beam section. The effective slab width of 24 in (600 mm) was adopted based on the AIJ Standard [24], which was used to determine the T-shaped beam section as well as the contribution of the slab steel in the effective slab width, as shown in **Fig. 4(c)**. In addition to that, constraints of some nodal DOFs of the joint macro element were introduced such that the opposite rigid plate of the beam-column joints should always be kept in parallel to consider the effect of in-plane constraints provided by the slab as a diaphragm.

**4.3 Boundary conditions, loading path and DOF constraints**

Boundary conditions were introduced into the numerical model to simulate the load pattern used in the laboratory tests. In the numerical model, a pin-support was provided at the base of the lower column segment, and horizontal rollers were introduced at the beam ends. The unidirectional and bidirectional lateral displacement cycles used in the laboratory tests were replicated in the simulation by using displacement control to apply lateral loads at the top of the column. To avoid a singular stiffness matrix due to the rotation of the whole structure around the vertical axis, the rotational displacement around the column axis at the column base was also constrained.

## 5. COMPARISON OF THE SIMULATED AND MEASURED RESPONSE

An original MATLAB script SICOJ was developed by the authors for the simulation of 3D fish bone structures subject to bi-directional lateral loading. The simulation is carried out on an ordinary PC. For the comparison, simulations with rigid beam-column joints are added for each case, where all the springs for concrete, steel and bond-slip within the joint block are set to be infinitely stiff and strong.

**5.1 Load-deflection relationship**

The test results and the simulations are compared in **Figures 12** through **14,** where the story shear vs. story drift relations for E-W and N-S directions are shown for the Specimens J1, J2 and

J3, respectively. For all specimens, the conventional rigid joint model was inadequate for predicting the strength, stiffness degradation, strength degradation and the observed highly pinched hysteretic response. The rigid joint model always overestimates the lateral strength, and the type of hysteretic behavior was masing-type, different from the test, where severe pinching was observed. Additionally, the rigid-joint model does not simulate the strength degradation due to bidirectional cyclic loading, which is observed for case Specimens J2 and J3. It is also noticed that the hysteretic loop of Specimen J1 shows an asymmetric curve. The simulations reproduce this behavior well, which may be attributed to residual tensile strain in the joint hoops at the last peak in the positive directional loading that diminishes the stiffness and strength of the beam-column joint at the loading path from the positive peak into the negative direction.

The models that include the 3D beam-column joint macro-element generally provide accurate simulations of the measured, stiffness and strength, hysteretic response, and degradation in stiffness and strength, which was observed for the specimens subjected to unidirectional and bidirectional lateral loading and for the specimens with and without two continuous beams framing into the joint.

However, close observation reveals some differences between the simulated and measured responses that may be attributed to the simple modeling of the slab as T-sections of a beam with fixed dimensions and a constant reinforcement contribution. Generally, the contribution of the effective slab to the strength and stiffness increases as the story drift demand increases. [25, 26] Therefore, the model could underestimate the strength and energy dissipation at large story drift. However, for Specimen J1, the simulation overestimates the peak strength and energy dissipation. This is attributed to overestimation of the effective slab width. Specimen J1 is a sub-assemblage from a one-way frame with no transverse beams. For this system, the contribution of the slab may be diminished. In contrast to this, the data show that the strength, initial stiffness and peak strength of Specimens J2 and J3 are accurately simulated for story drift demands of less than 2%. However, the strength and energy dissipation at story drift of 4% are significantly underestimated. This may be attributed to the true slab effective width increase with increasing deformation demand.
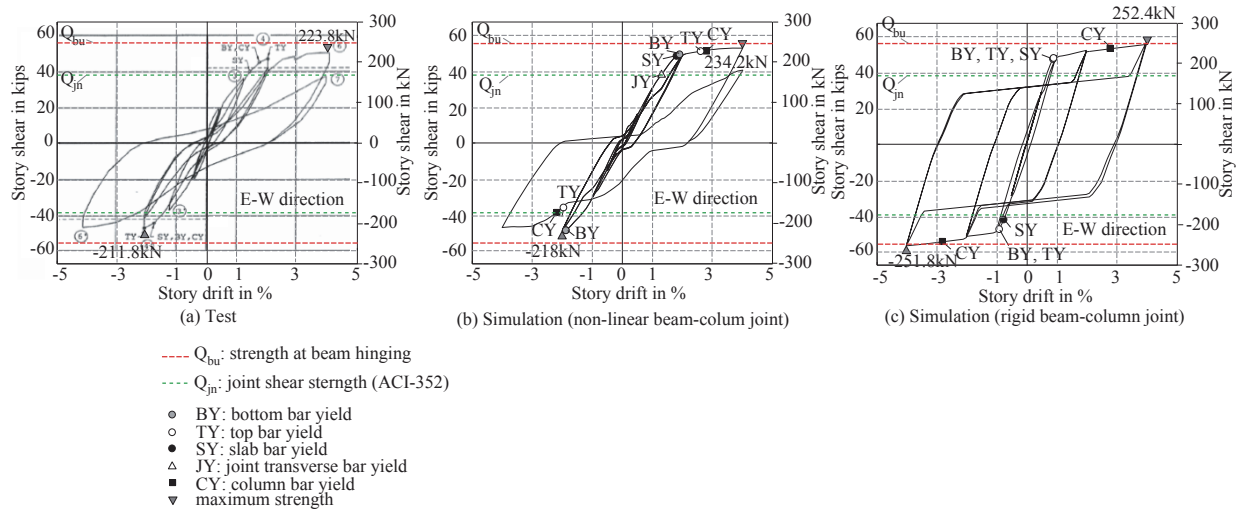


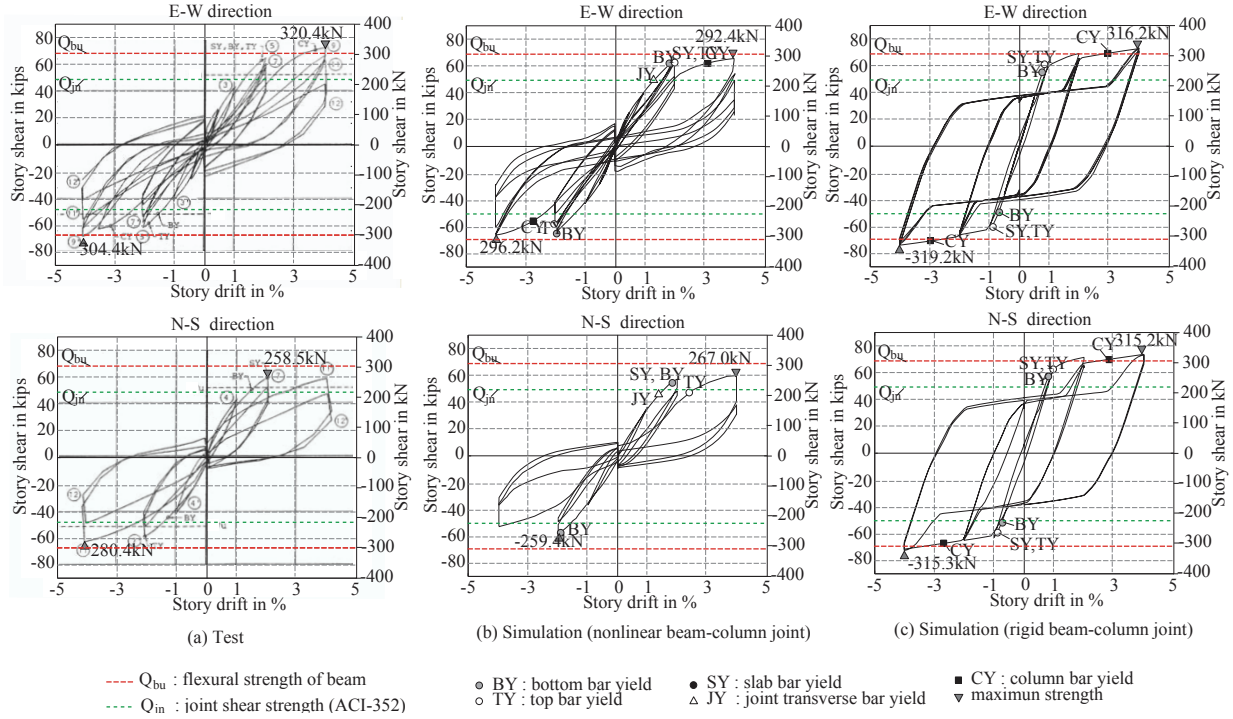**Fig. 12** – Story shear-story drift relationship of Specimen J1

16

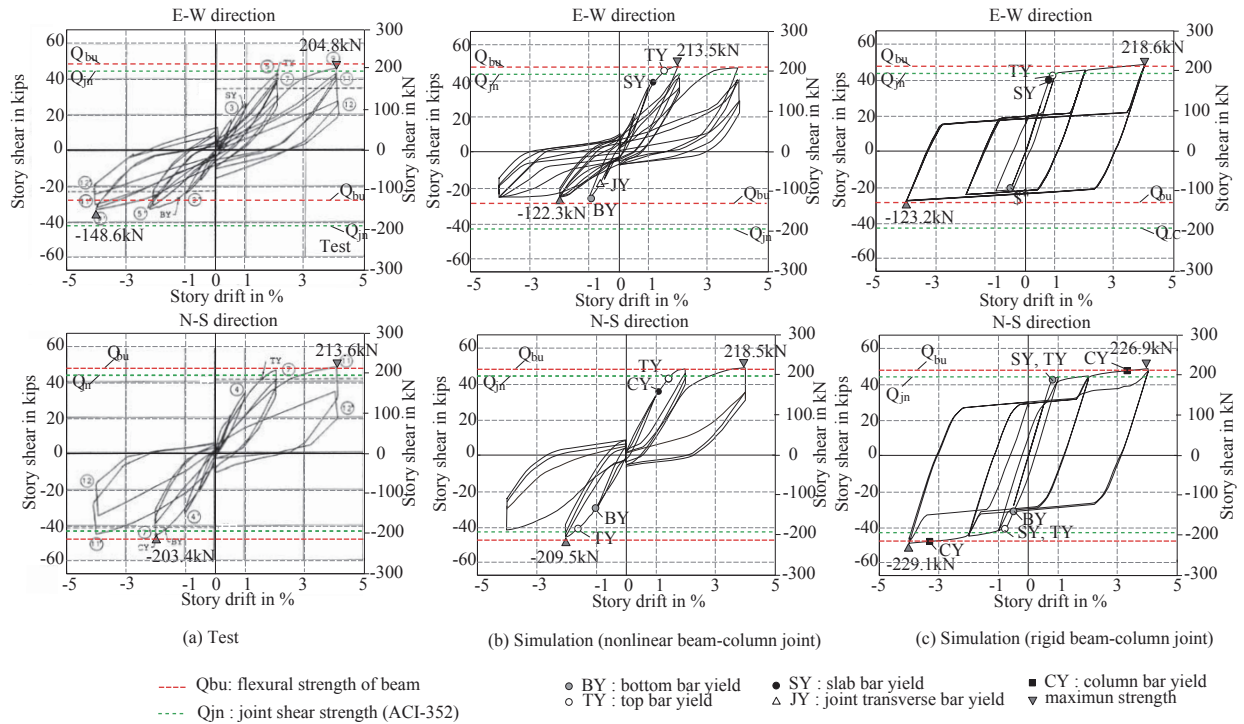**Fig. 13 –** Story shear-story drift relationship of Specimen J2



**Fig. 14 –** Story shear-story drift relationship of Specimen J3

**5.3 Failure Mode**

Researchers at the University of Texas at Austin reported [12] the failure of Specimens J1, J2 and J3 as joint shear failure following flexural yielding of the beams. The failure mode by the simulation with the macro element is consistent with the test data. In **Fig. 12** through **Fig. 14**, the first yielding of joint transverse reinforcement, beam longitudinal reinforcement, and column longitudinal reinforcement are marked for both the measured and simulated response histories. In the analyses of Specimen J2, the yielding of the beam longitudinal reinforcement occurred at 2% story drift, and yielding of the column longitudinal reinforcement occurred at 4% story drift under unidirectional loading conditions. **Figure 15** shows story shear versus joint shear distortion as measured and as simulated for specimen J1. The response simulated using the 3D macro-element shows good correlation with experimental data. The results for Specimens J2 and J3 are not shown, but similar correlations between the simulated and measured response were observed. In general, the contribution of joint shear distortion to total story drift ratio as well as the sequence of yielding for beam and column longitudinal reinforcement and joint transverse reinforcement were accurately predicted by the model. Thus, the 3D beam-column joint macro-element is considered to provide reliable and accurate simulation of the response for unidirectional and bidirectional lateral loads.
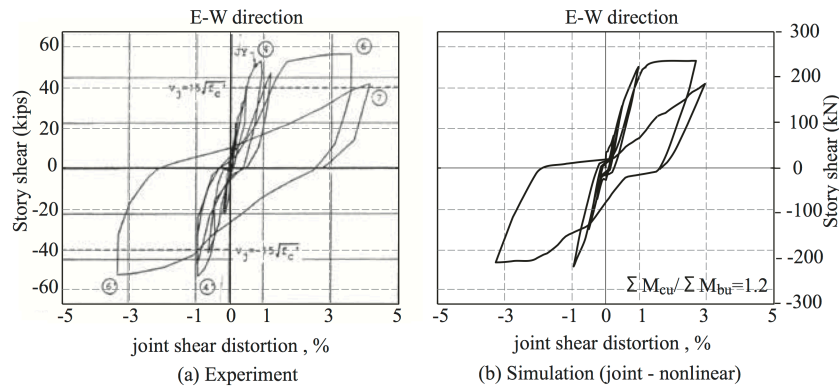


Fig. 15 – Story shear-joint distortion relationship for Specimen J1

**5.4 Story Shear Response Trajectories**

**Figures 16** and **17** present calculated and measured story shear trajectories for Specimens J2 and J3 for the cases of 2% and 4% story drift, respectively. The data show that the conventional rigid joint model is inadequate in all cases. The ACI-352 provision for joint shear strength underestimates the test results in particular under 45 degree directional loading. It means that bidirectional loading is necessarily the reason for the increase of joint shear damage. Thus, existing joint shear strength models are inappropriate for estimating joint shear strength. In contrast, the beam-column joint macro-element model provides accurate simulation of the measured story shear trajectories, i.e., the joint shear strength in the 45 degree direction as well as the 0 and 90 degree directions agree with test, and the story shear resistance under restrained story drift always decreases during loading or unloading in the transverse direction. In general, the calculated story shear trajectory is fairly consistent with the measured response for all quadrants of the load trajectory; however, there is some loss of capacity in the second cycle of loading to a given drift level. Thus, the numerical analyses simulate well the strength loss under bidirectional lateral loading.
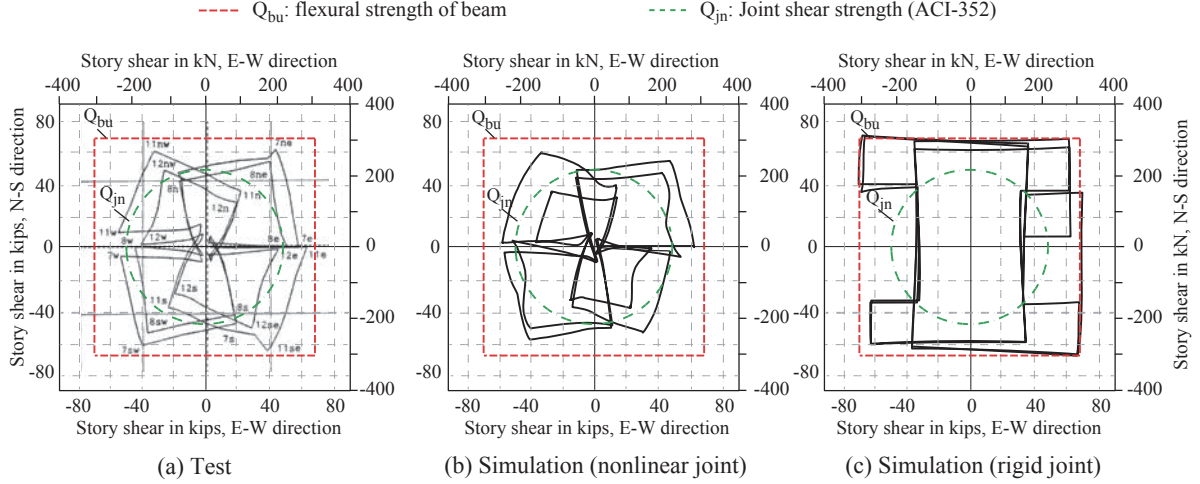
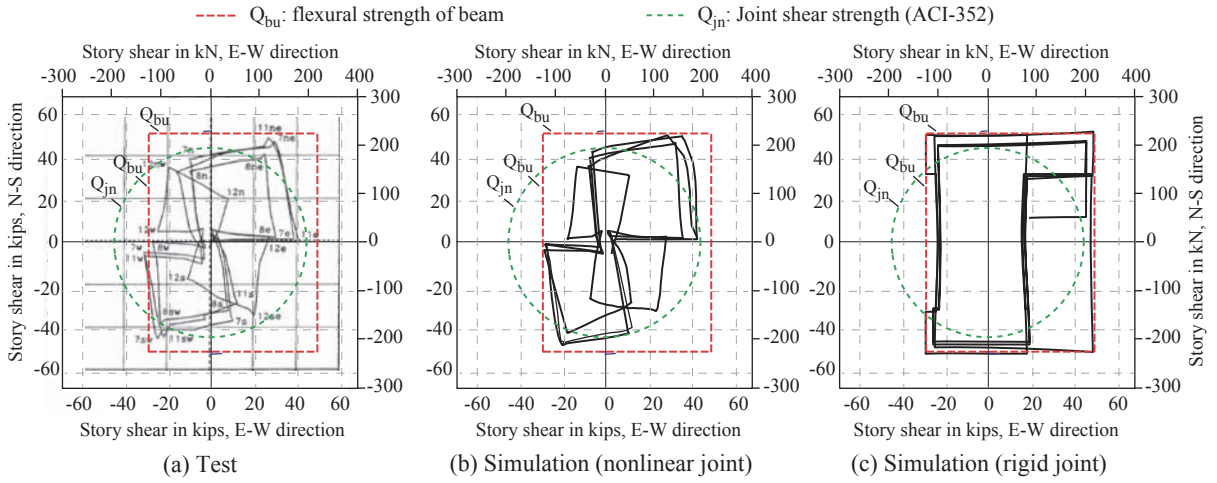Fig. 16 – Story shear orbit of Specimen J2



Fig. 17 – Story shear orbit of Specimen J3

## 6. CONCLUSIONS

The research presented here shows that the proposed 3D joint macro-element can satisfactorily simulate the observed strength, stiffness and hysteretic behavior of 3D beam-column joints, including the strength degradation resulting from cyclic bidirectional lateral loading. The 3D joint macro-element consists of six independent rigid plates and multiple uniaxial springs. The springs represent the concrete, reinforcing steel and bond-slip behavior between concrete and reinforcing bars. The 3D joint macro-element was used to simulate the response of one beam-column joint sub-assemblages and two slab-beam-column joint sub-assemblages tested by researchers at UT Austin. The specimens were subjected to quasi-static cyclic bidirectional and unidirectional lateral loading. Comparison of the simulated and measured response histories shows that the simulated histories are in good agreement with the observed cyclic behavior and that the proposed model provides significantly better simulation of response than the rigid joint model typically used. The data show that for unidirectional and bidirectional lateral loading, the macro-

element is capable of reproducing the pinching, stiffness degradation and strength deterioration that results from cyclic loading.

Implementation of this model in software for non-linear time-history analysis of concrete frames offers the potential for better estimation of the 3D seismic response of the ductile moment resisting reinforced concrete frames with one-way and two-way framing systems. For two-way systems comprising the slab, beams and columns, modeling considering the effect of the slab contribution to joint strength and beams is critical for the response simulation.

When assessment of the building frame's earthquake performance with two-way ductile RC moment-resisting frames and continuous slabs is necessary, the proposed macro-element is the straightforward and practical option for performance assessment, including assessment of the impact of bidirectional cyclic loading on maximum response and collapse vulnerability.

Continuing research on 3D beam-column joint test and model validation are necessary to reveal the limitation of the model not shown in the paper, which include failure modes, the geometry of the joint, column axial stiffness. That is necessary to be done in the future study.

## 7. ACKNOWLEDGMENTS

## 8. REFERENCES

1.  Pampanin, S., Magenes G. and Carr, A. (2003). Modelling of shear hinge mechanism in poorly detailed RC Beam-column Joints. Athens, Greece: fib 2003 Symposium "Concrete Structures in Seismic Regions", May 2003. Paper n.171.
2.  Altoontash, A. (2004). Simulation and Damage Models for Performance Assessment of Reinforced Concrete Beam-Column Joints. PhD Dissertation, Department of Civil and Enviornment Engineering, Stanford University, Stanford, California. 2004.
3.  Ghobarah, A. and Biddah, A. (1999). Dynamic analysis of reinforced concrete frames including joint shear deformation. Engineering Structures, Volume 21, Issue 11, November 1999, Pages 971–987.
4.  Lowes, L. N. and Altoontash, A. (2003). Modeling Reinforced-Concrete Beam-Column Joints Subjected to Cyclic Loading," Journal of Structural Engineering, Vol. 129, No. 12, December 1, 2003, pp. 1686-1698.
5.  Shin, M. and LaFave, J. M. (2004). Testing and Modeling for Cyclic Joint Shear Deformations in RC Beam-column Connections. *Proceedings of the Thirteenth World Conference on Earthquake Engineering*, August 1–6, 2004, Vancouver, B.C., Canada, Paper No. 0301.

6. Shiohara, H., (2001), New Model for Shear Failure of RC Interior Beam-Column Connections, Journal of Structural Engineering, ASCE, Volume 127, Issue 2, February 2001, pp. 152-160.

7. Tajiri, S.; Shiohara, H.; and Kusuhara, F. (2006). A New Macro Element of Reinforced Concrete Beam-Column Joint for Elasto-Plastic Plane Frame Analysis," *Proceedings of the 8th U.S. National Conference on Earthquake Engineering*, San Francisco, April 18-22, 2006, paper No. 674.

8. Kusuhara, F.; Kim, S.; and Shiohara, H. (2013). Seismic Response of Reinforced Concrete Moment Resisting Frames of Beam-Column Joint Yielding. *Journal of Structural and Construction Engineering of AIJ*, Architectural Institute of Japan, Tokyo, Japan, Vol. 78, No. 686, April 2013, pp. 847-855. (in Japanese)

9. Hitoshi Shiohara. (2012). Reinforced Concrete Beam-column Joints: An Overlooked Failure Mechanism. ACI Structural Journal, Vol. 109, No. 1, January-February, 2012, pp. 65-74.

10. Shiohara, H. and Kusuhara, F. (2014). The Next Generation Seismic Design for Reinforced Concrete Beam-column Joints. Proc. Tenth U.S. National Conference on Earthquake Engineering, July 21-25, 2014, Anchorage, Alaska, DOI: 10.4231/D3T727G8S

11. Roberto, L. (1983). The Influence of Floor Members on the Behavior of Reinforced Concrete Beam-column Joints subjected to Severe Cyclic Loading. PhD Thesis, the University of Texas at Austin, December 1983, 323pp.

12. Kurose, Y., and Jirsa, J. O. (1988). Study of Reinforced Concrete Beam-Column Joints Under Uniaxial and Biaxial Loading. *PMFSEL Report* No. 88-2, The University of Texas at Austin, 1988, 146 pp.

13. Park, Sangjoon; Mosalam Khalid M. (2012). Experimrental and Analytical Studies on Reinforced Concrete Buildings with Seismically Vulnerable Beam-column Joints, PEER Report 2012/03, Pacific Earthquake Engineering Research Center, October 2012, 194pp.

14. Suzuki, N., Aoyama, H. and Otani, S. (1982). Experimental Study of Three Dimensional Reinforced Concrete Beam-Column Joints: Part 1. *Transactions of AIJ*, Architectural Institute of Japan, Tokyo, Japan, August 1982, pp. 1655-1656. (in Japanese)

15. Park, R.; Priestley, M. J. N.; and Gill, W. D. (1982). Ductility of Square-Confined Concrete Columns. *Proceeding of the American Society of Civil Engineers*, Vol. 108, No. ST4, April 1982, pp. 929-950.

16. Nakamura, H., and Higai, T. (2001). Compressive Fracture Energy and Fracture Zone Length of Concrete. *Modeling of Inelastic Behavior of RC Structures under Seismic Loads*, ASCE, 2001, pp. 471-487.

17. Concrete Committee of Japan Society of Civil Engineers (2007). Standard Specifications for Concrete Structure-2007 (English Version)," Japan Society of Civil Engineers, 2007, pp. 48-49.

18. Eligehausen, R.; Popov, E. P.; and Bertero, V. V. (1982). Local Bond Stress-Slip Relationships of Deformed Bars under Generalized Excitations," Proceedings of the 7th European Conference on Earthquake Engineering, Athens, Greece, Vol. 4, 1982, pp. 69-80.

19. Morita, S., and Kaku, T. (1975). Bond-Slip Relationship under Reversed Cyclic Loading," *Transactions of AIJ*, Architectural Institute of Japan, Tokyo, Japan, No.229, March 1975, pp. 15-24. (in Japanese)

20. Comite Euro-International du Beton (1991). CEB-FIP Model Code 1990," July 1991.

21. ACI Committee 318 (1983). Building Code Requirements for Reinforced Concrete (ACI 318-83). American Concrete Institute, Farmington Hills, MI, 1983, 111pp.

22. Joint ACI-ASCE Committee 352 (1985). Recommendations for Design of Beam-Column Joints in Monolithic Reinforced Concrete Structures (ACI 352 R-85). American Concrete Institute, Farmington hills, MI, 1985, 37 pp.

23. Scott, M., and Fenves, G. (2006). Plastic Hinge Integration Methods for Force-Based Beam-Column Elements. *Journal of Structural Engineering*, American Society of Civil Engineers, Vol. 132, No. 2, February 2006, pp. 244–252.

24. Architectural Institute of Japan, Structure Committee (2010). Standards for Structural Calculation of Reinforced Concrete Structures," AIJ, Tokyo, Japan, 2010, 525 pp. (in Japanese)

25. Yoshimura, M., Kurose, Y. and Kaminosono, T. (1988). Nonlinear Behavior of Beam and Column Members Observed in the Test of the Full-scale Reinforced Concrete Seven-Story Structure − U.S.-Japan Cooperative Research Program Part 5 −, *Journal of Structural and Construction Engineering of AIJ*, Architectural Institute of Japan, Tokyo, Japan, No. 391, September 1988, pp. 27-35. (in Japanese)

26. Pantazopoulo, S. J., Moehle, J. P. and Shahrooz, B. M. (1988). Simple Analytical Model for T-Beams in Flexure, *Journal of Structural Engineering*, Vol. 114, No. 7, July 1988, pp. 1507-1523.